Jérôme Bürgi, Pascal Lill, Evdokia-Anastasia Giannopoulou, Cy M. Jeffries, Grzegorz Chojnowski, Stefan Raunser, Christos Gatsogiannis* and Matthias Wilmanns*

Asymmetric horseshoe-like assembly of peroxisomal yeast oxalyl-CoA synthetase

https://doi.org/10.1515/hsz-2022-0273
Received September 5, 2022; accepted December 17, 2022;
published online January 26, 2023

Abstract: Oxalyl-CoA synthetase from *Saccharomyces cerevisiae* is one of the most abundant peroxisomal proteins in yeast and hence has become a model to study peroxisomal translocation. It contains a C-terminal Peroxisome Targeting Signal 1, which however is partly dispensable, suggesting additional receptor bindings sites. To unravel any additional features that may contribute to its capacity to be recognized as peroxisomal target, we determined its assembly and overall architecture by an integrated structural biology approach, including X-ray crystallography, single particle cryo-electron microscopy and small angle X-ray scattering. Surprisingly, it assembles into mixture of concentration-dependent dimers, tetramers and hexamers by dimer self-association. Hexameric particles form an unprecedented asymmetric horseshoe-like arrangement, which considerably differs from symmetric hexameric assembly found in many other protein structures. A single mutation within the self-association interface is sufficient to abolish any higher-level oligomerization, resulting in a homogenous dimeric assembly. The small C-terminal domain of yeast Oxalyl-CoA synthetase is connected by a partly flexible hinge with the large N-terminal domain, which provides the sole basis for oligomeric assembly. Our data provide a basis to mechanistically study peroxisomal translocation of this target.

Keywords: oligomeric self-assembly; oxalyl-CoA synthetase; peroxisomal translocation.

Introduction

Oxalyl-CoA synthetase (OCS) is an acyl-CoA synthetase found in fungi and plants, but not in the vertebrate kingdom (Foster and Nakata 2014). OCS-catalyzed formation of oxalyl-CoA is crucial to prevent cellular toxicity due to accumulation of oxalic acid (Williams and Smith 1968). In contrast to plant oxalyl-CoA synthetases, the fungal enzymes comprise a C-terminal Peroxisome Targeting Signal 1 (PTS1) motif and hence are targets for translocation into peroxisomes. In yeast, OCS, also known as Pcs60, is one of the most abundant proteins in peroxisomes under conditions where peroxisome function is essential, such as growth in oleate (Blobel and Erdmann 1996).

OCS belongs to the acyl-CoA synthetase superfamily of adenylate forming enzymes (ANL) (Foster and Nakata 2014). Acyl-CoA synthetases are composed of two domains: a larger N-terminal domain (NTD) that comprises the active site, and a smaller C-terminal domain (CTD) that covers the NTD active site cleft upon substrate binding. Enzymes from the ANL family synthesize their products in a two-step reaction that requires a well characterized domain alternation mechanism (Gulick 2009; Gulick et al. 2003). The mechanism is associated with significant conformational changes, which involves a major rotation of the NTD/CTD arrangement.

To date, OCS structural characterization has remained limited to the non-peroxisomal *Arabidopsis (A.) thaliana* and *Lathyrus (L.) sativus* enzymes (Fan et al. 2016; Goldsmith et al. 2022). As the structure of *L. savitus* OCS was only determined in the presence of AMP, we have focused structural comparison on the *A. thaliana* enzyme, which was also determined in the apo conformation. Yeast OCS has

Jérôme Bürgi and Pascal Lill contributed equallly to this work.

***Corresponding authors: Christos Gatsogiannis**, Department of Structural Biochemistry, Max Planck Institute of Molecular Physiology, D-44227 Dortmund, Germany; and Institute for Medical Physics and Biophysics and Center for Soft Nanoscience, University of Münster, Busso-Peus-Str. 10, D-48149 Münster, Germany, E-mail: christos.gatsogiannis@uni-muenster.de. https://orcid.org/0000-0002-4922-4545; and **Matthias Wilmanns**, European Molecular Biology Laboratory, Hamburg Unit, Notkestrasse 85, D-22607 Hamburg, Germany; and University Hamburg Clinical Center Hamburg-Eppendorf, University Hamburg, D-20251 Hamburg, Germany, E-mail: matthias.wilmanns@embl-hamburg.de. https://orcid.org/0000-0002-4643-5435
Jérôme Bürgi, Evdokia-Anastasia Giannopoulou, Cy M. Jeffries and Grzegorz Chojnowski, European Molecular Biology Laboratory, Hamburg Unit, Notkestrasse 85, D-22607 Hamburg, Germany. https://orcid.org/0000-0003-1171-3455 (J. Bürgi)
Pascal Lill, Department of Structural Biochemistry, Max Planck Institute of Molecular Physiology, D-44227 Dortmund, Germany; and Institute for Medical Physics and Biophysics and Center for Soft Nanoscience, University of Münster, Busso-Peus-Str. 10, D-48149 Münster, Germany
Stefan Raunser, Department of Structural Biochemistry, Max Planck Institute of Molecular Physiology, D-44227 Dortmund, Germany

become a model for PTS1 mediated cargo import, in which the PTS1 motif may become dispensable for peroxisomal receptor Pex5 binding but not import into peroxisomes, indicating a second non-PTS1 bindings site (Hagen et al. 2015). Based on these findings, we became curious about specific structural features of the peroxisomal enzyme, which may act favorably in promoting peroxisomal translocation. Surprisingly, by using X-ray crystallography, we found *Saccharomyces (S.) cerevisiae* OCS to be arranged in an asymmetric three-fold repeated layer of homodimers, which form a hexamer with an overall horseshoe shape. Using single particle cryo-electron microscopy (cryo-EM) and Small Angle X-ray Scattering (SAXS), we confirmed that yeast OCS forms concentration-dependent single, double and triple-layered homo-dimeric assemblies with an overall configuration consistent with our X-ray crystallography data. A single mutation in OCS is sufficient to abolish the ability of OCS to form multiple layers of homodimers, which allowed us to characterize homogenous single layer OCS homo-dimeric species. In addition, we observed that *S. cerevisiae* OCS homodimerization is different from the *A. thaliana* enzyme and thus non-conserved. Finally, and again in contrast to *A. thaliana* OCS, the CTD in *S. cerevisiae* OCS is only in a loose arrangement with the NTD. Our data suggest that – unless these features have evolved for different functional reasons – they could play a role in promoting efficient *S. cerevisiae* OCS translocation into peroxisomes.

Results

Yeast OCS forms an asymmetric three-layered hexameric assembly

To understand the structural arrangement of yeast OCS, we first determined the crystal structure of the enzyme at 2.9 Å resolution (Figure 1, Supplementary Table S1). Within each asymmetric unit of these crystals, we found two hexameric assemblies with an identical arrangement, composed of trimers of dimers (Figure 1A, Table 1, Supplementary Figure S1).

While the electron density of all N-terminal domains (NTD) of the two OCS hexamers was well interpretable for the complete NTD sequence, the density accounting for the smaller CTD was less well defined to various degrees. We quantified the expected density for each CTD by map-model correlation analysis, revealing correlation coefficients (cc) between 0.15 and 0.83 (Table 2). As an analysis of contacts with symmetry-related OCS molecules did not reveal major differences, the varying levels of CTD density are a likely a consequence of inherent flexibility of the OCS NTD/CTD arrangement, in-line with previous findings of other members of the ANL family (Gulick 2009). To this end, we used cc = 0.7 as a threshold for structural interpretation, to model two CTDs of the first OCS hexamer (chains D1(A) and D2(B)) and one CTD of the second OCS hexamer (chain D2(A)). Due to limited interpretable density, the CTD sequences that were modeled remained fragmented (Table 2). Modeling of these three CTDs allowed us to assigning OCS residues 1–429 to comprise the NTD, followed by a seven-residues flexible hinge segment (430–436), which connects to the CTD (residues 437–543). As the PTS1 motif required for peroxisome targeting is at the C-terminus it is not visible in any of our structures (Supplementary Figure S1).

The three OCS dimers found in both hexamers assemble into an unusual three-fold repeated stack, forming a horseshoe-like arrangement (Figure 1A, Supplementary Figure S1). This assembly is composed of two orthogonal layers where each of the three two-fold symmetry related OCS homodimers contribute one protomer to the first layer and the other protomer to the second layer, thus generating an asymmetric trimer of OCS dimers. The three-fold repeated OCS dimer layers are related by rotational angles between pairs of OCS dimers 1/2 and 2/3 of about 113° each (Figure 1A, Table 1), thus considerably deviating from three-fold symmetry. The two OCS layers with three protomers each are in congruent positions when looking along the pseudo-threefold axis. Within this OCS dimer layer arrangement, OCS dimers 1 and 2 as well as OCS dimers 2 and 3 interact via relatively small two-fold repeated interfaces of about 400 Å^2 each (Figure 1B, Table 1, Supplementary Table S4). In these two virtually identical OCS dimer/dimer interfaces, we found a single side chain-specific salt bridge between D36 and K352 (Figure 1C). As result of these dimer/dimer arrangements involving OCS dimer 1 /dimer 2 and OCS dimer 2 /dimer 3, there is a deep and narrow groove between OCS dimers 1 and 3 (Figure 1A, left panel). The visible CTDs are not involved in any of these interfaces. In addition, each of the three OCS homodimers are formed through an elongated and two-fold symmetric interface of around 1100 Å^2 between OCS NTDs, supported by an array of distinct specific interactions (Figure 2A–B). The overall dimensions of the NTD OCS hexameric arrangement are about 11 nm within each of the two trimeric OCS layers and 9 nm across the trimeric OCS layers (Figure 1A). When including the modeled CTDs the overall particle size increases to about 14 nm × 11 nm, respectively.

To investigate the OCS dimer module as a separate entity, we converted the positive charge of K352, which forms

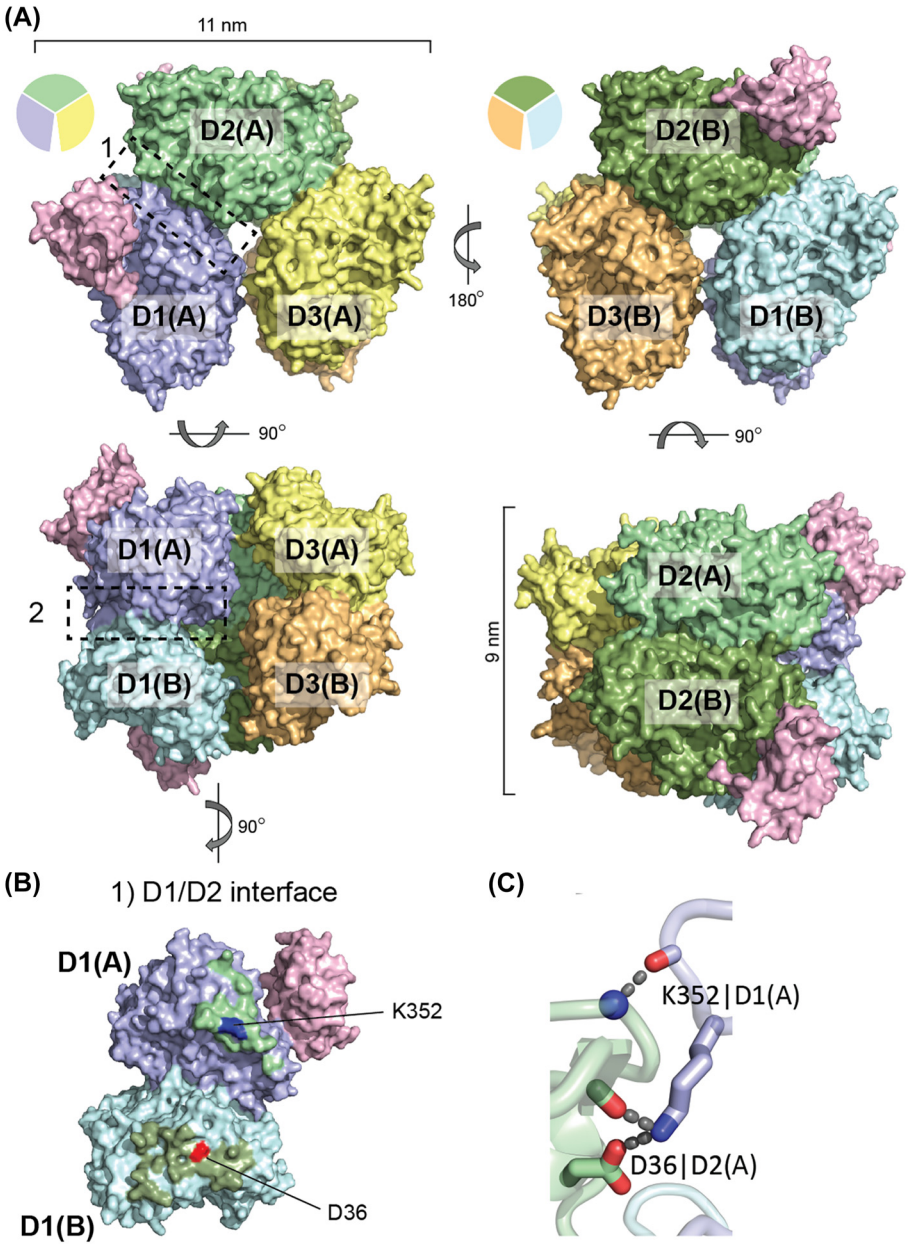

Figure 1: X-ray crystal structure of the hexameric OCS (*wt*) assembly. (A) Three OCS dimers associate into an asymmetric hexameric assembly with a horseshoe-like overall shape. OCS dimer-1 protomers D1(A) and D1(B) are colored in marine blue and cyan, respectively; D2(A) and D2(B) in green and dark green, respectively; D3(A) and D3(B) in yellow and orange, respectively. Upper panel: View along a pseudo-threefold axis in two opposite orientations. As the protomers of the three OCS dimers are related by two-fold symmetry orthogonal to the pseudo-threefold axis, only the front layer of the three OCS dimers is visible. For the purpose of clarity, the visible OCS protomers are indicated by pie charts in the same colors and the angles, defining the relations between the three OCS dimers (*cf*. Table 2). Two CTDs out of six OCS protomers were included into the overall structure of the OCS hexamer-1, used in this illustration (in light pink). The OCS hexameric assemblies in the lower panel are rotated by 90° around a horizontal axis with respect to the upper panel. Due to the overall horseshoe-like arrangement, a long deep crevice generated by the OCS hexameric assembly becomes visible (lower left panel). The overall dimensions of the OCS hexameric assembly are indicated as well. (B) Molecular details of OCS dimer/dimer assembly, exemplified for the D1/D2 interface indicated by box 1 in panel A. The D2/D3 interface is virtually identical (Table 1). Colors for dimer D1 are as in panel A. Surface areas of dimer D1 that are in contact with dimer D2 are shown in the colors used for D2. Polar residues that contribute to specific dimer D1/D2 interface interactions are colored by their side chain charges (negative, red; positive, blue) and are labeled. The only sidechain specific polar interaction between D1 and D2 is generated by D26 and K352 and is two-fold repeated with opposite orientations, involving D1(A)/D2(A) and D1(B)/D2(B). The respective surface areas on D1(A, B) are boxed. (C) The D36-K352 interaction is supported by additional hydrogen bonds with the OCS main chain backbone (right panel).

Table 1: OCS oligomeric assembly.

OCS (*wt*) Dimeric assembly	Rotation [deg.]	Interface protomers A/A [A^2]	Interface protomers B/B [A^2]	Total interface [A^2]
D1	180			1009
D2	180			1013
D3	180			1020
Hexameric assembly				
D1/D2	113.5	398	397	795
D2/D3	113.5	397	392	789
D3-D1	133	24	15	39
OCS (KD)				
D1	180			1031

Further details on distances of specific interface interactions are listed in Supplementary Table S4.

Table 2: OCS NTD/CTD arrangement flexibility.

Subunit	CC[a]	CTD sequence modelled[b]	Δ(Θ) NTD/CTD Θ D1(A) = 0°[c]
OCS (*wt*) hexamer-1			
D1(A)	0.83	443–533	0.0
D1(B)	0.59		
D2(A)	0.36		
D2(B)	0.76	443–519	10.0
D3(A)	0.17		
D3(B)	0.31		
OCS (*wt*) hexamer-2			
D1(A)	0.21		
D1(B)	0.41		
D2(A)	0.70	443–467, 474–532	117.8
D2(B)	0.34		
D3(A)	0.27		
D3(B)	0.17		
OCS (KD) dimer			
D(A)	0.78	443–478, 489–507	n.d.
D(B)	0.53		

[a]Correlation coefficient (CC), as described in the materials and methods section. [b]Residue numbers as specified in P38137 (UNIPROT). [c]Calculated with DynDom (Lee et al. 2003).

the salt bridge across the OCS dimer protomer interface, into a negative charge by mutating it to aspartate (Figure 1C). As predicted, the OCS K352D (KD) variant lost its ability to form a hexameric assembly as seen by a delayed elution volume by size exclusion chromatography (Figure 2A). We then solved the X-ray crystal structure of the KD mutant to 2.5 Å resolution. In the crystal structure, the OCS (KD) variant forms a homodimer, which is identical to the one observed in the OCS (wild-type, *wt*) hexameric structure (Figure 1A, Figure 2B–C). Due to higher resolution of the structure of the OCS (KD) variant, atomic B factor refinement allowed insight into the mobility distribution of the overall OCS fold. As expected, the so-called P-loop, which has a crucial role in nucleotide binding of members of the ANL family (Gulick 2009) belongs to the most flexible segments of the catalytic NTD (Supplementary Figure S2). Similar to our observations in the hexameric OCS assembly there was only sufficient density for model building of a partially resolved CTD of one of the OCS protomers, supporting a semi-flexible arrangement of the NTD relative to the CTD in the crystal lattice (Figure 2C). At this point we analyzed the nature of the NTD/CTD positions of all OCS protomers where it was possible to assign density to the CTD. While the arrangements of two OCS promoters of the *wt* hexameric assembly and of the OCS (KD) variant are identical, the CTD of the third OCS protomer with modeled CTD is rotated by 118° when using the first NTD/CTD arrangement as reference (Figure 2D, Table 2). The rotation is due to major changes of the dihedral angles of residues 433–435 within the NTD/CTD-connecting flexible hinge. Both arrangements are characterized by a scarce number of interactions between residues from the NTD and CTD (Figure 2D). While the first arrangement has a single hydrogen bond between main chain carbonyl group of T430 (NTD) and S445 (CTD) in common (Figure 2D, left panel), the second NTD/CTD arrangement is held by a specific interaction between the tyrosine hydroxyl group of Y420 from the NTD and T519 and T521 from the CTD, close to the OCS C-terminus (Figure 2D, right panel). The latter two residues are not visible in some of the OCS protomers with the first NTD/CTD arrangement (Table 2). When comparing the two arrangements, for instance the positions of T519/T521 are different by about 3 nm on those superimposed protomers. This illustrates the scale of movement induced through this rotation (Figure 2D).

OCS dimeric layer self-assembly is concentration-dependent

We independently determined the structure of OCS by single particle cryo-EM (Figure 3, Supplementary Figure S3, Supplementary Table S2). After motion correction, the micrographs showed a homogeneous spread of globular particles (Supplementary Figure S3A–B), hinting towards OCS oligomers comprised of multiple copies of OCS homodimers. In addition to hexameric OCS accounting to 63% of all particles, we also detected populations of smaller particles with 33% associated with OCS tetramers

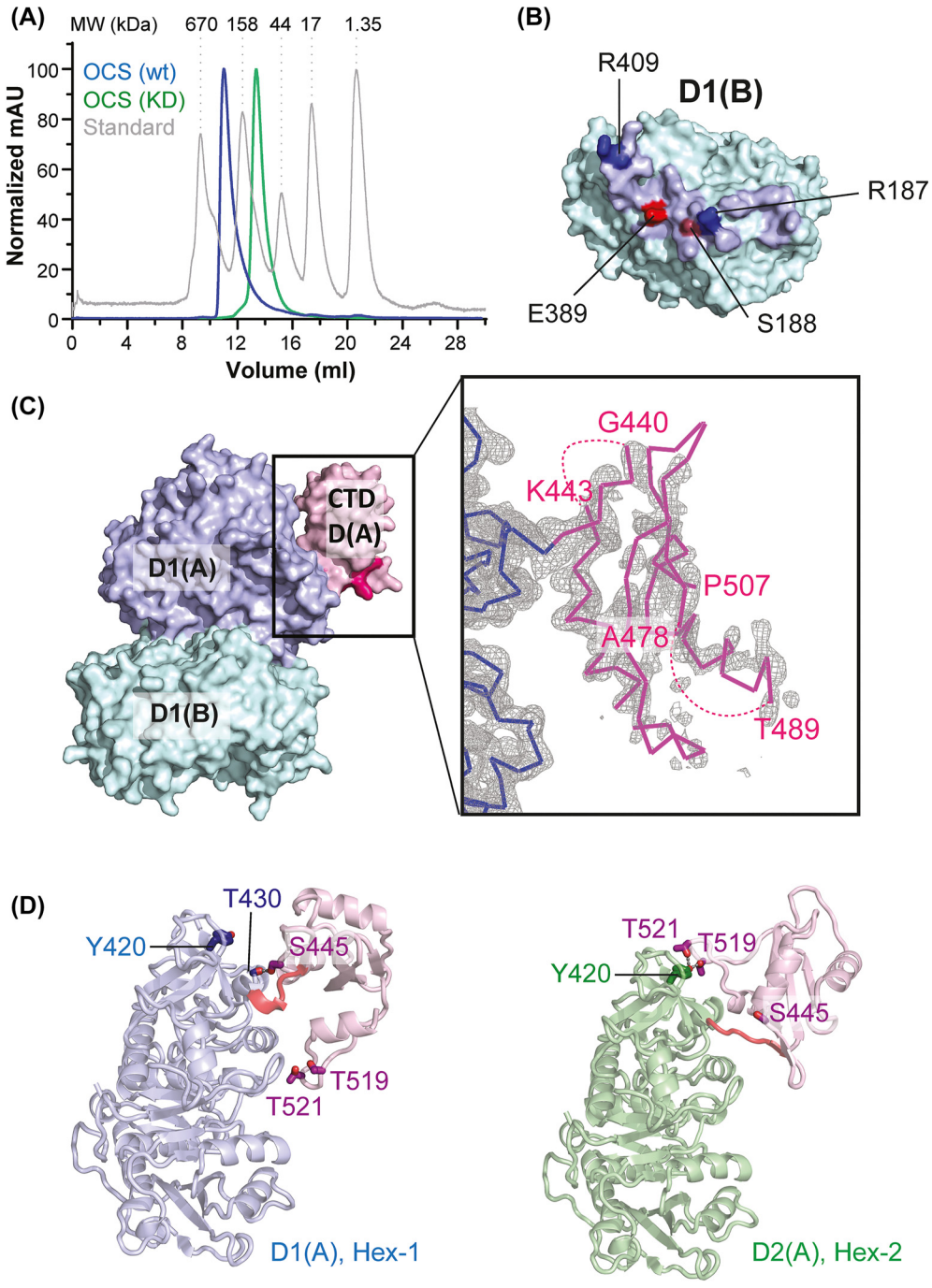

Figure 2: X-ray structure of the dimeric OCS (KD) mutant assembly: (A) Size exclusion profiles of hexameric OCS (*wt*, blue) and dimeric K352D (KD, green). Calibration standards are shown as well. (B) Dimer interface of the KD variant, which is identical to the interfaces of the three dimers D1, D2 and D3 of the OCS (*wt*) hexameric assembly (*cf*. Figure 1). The colors are identical to those used for dimer D1 in the hexameric OCS (*wt*) assembly (Figure 1). Polar residues that contribute to specific dimer interface interactions are labeled. (C) Surface presentation of the dimeric OCS (KD) variant. The OCS CTD is visible in only in one of the two protomers of the OCS (KD) dimer (light pink). The NTD/CTD hinge region is colored in hot pink. Boxed inlet: Composite *2Fo-Fc* OMIT map of the OCS (KD) D1(A) CTD in ribbon presentation. The boundaries of visible CTD fragments are labeled (*cf*. Table 2). (D) Molecular details of NTD/CTD interface of protomer D1(A) of the *wt* OCS hexamer-1 (left panel) and of protomer D2(A) of the *wt* OCS hexamer-2 (right panel). The CTD of D2(A) of the *wt* OCS hexamer-2 is rotated by 118° with respect to the orientation of th CTD of D1(A) of the *wt* OCS hexamer-1 (*cf*. Table 2). This change is most significantly visualized by CTD residue positions T519 and T521, which are involved in specific interactions with the NTD in the second conformation only (right panel). The NTD/CTD arrangements found in protomer D2(B) of *wt* OCS hexamer-1 and D(A) of the OCS (KD) variant are similar to that of protomer D1(A) of the *wt* OCS hexamer-1 (left panel) (*cf*. Table 2, Supplementary Figure S1).

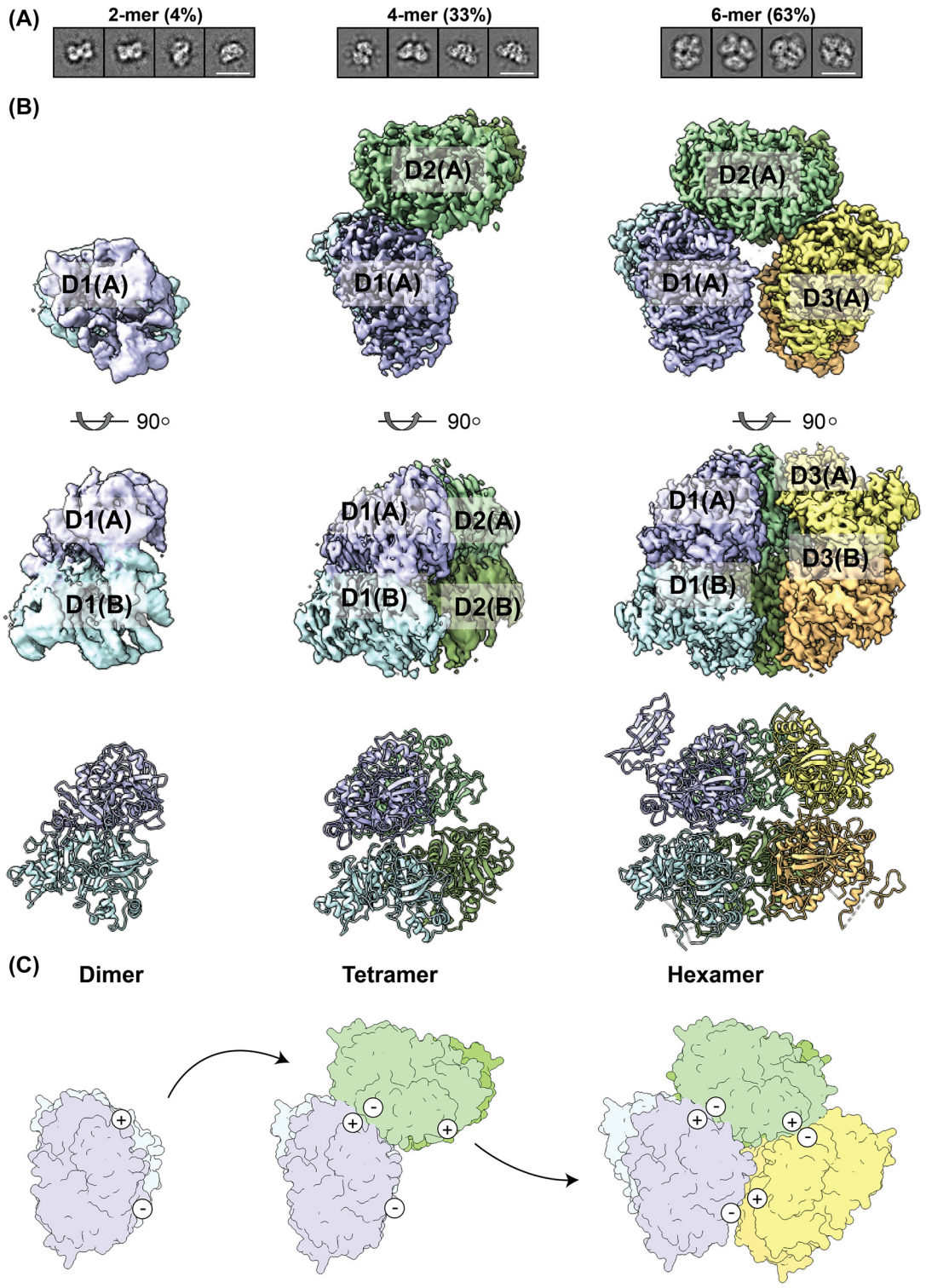

Figure 3: Cryo-EM structures of hexameric, tetrameric and dimeric OCS assemblies. (A) Representative cryo-EM 2D class averages of OCS (*wt*) dimeric, tetrameric and hexameric assemblies, with the percentage of particles for each oligomeric assembly indicated. (B) Density maps of dimeric (left panel), tetrameric (central panel) and hexameric (right panel) OCS (*wt*) cryo-EM samples in two orientations, rotated by 90° around a horizontal axis. The density map colors and labels are as in Figure 1. For comparison, structural cartoons of these assemblies are shown below. (C) Scheme indicating a plausible OCS dimer self-assembly path based on the distribution of cryo-EM particles and biophysical data (*cf*. Figure 4). Dimeric OCS self-assembly requires the formation of a two-fold repeated salt bridge between neighboring OCS dimers (*cf*. Figure 1). According to this scheme, OCS dimer self-assembly beyond the observed hexameric arrangement is not permissive, as this would lead to steric clashes.

and 4% with OCS dimers (Figure 3A). The 2D class averages accounting for the hexameric assembly revealed a large complex with the same characteristic horseshoe-like assembly as observed in the crystal structure (Figure 3A, right panel, Figure 1).

For the hexameric OCS assembly, we obtained a 3D reconstruction at an average resolution of 3.1 Å (Figure 3B, right panel, Supplementary Figure S4B), which agrees well with the crystal structure. Hence, the complete crystallographic hexameric complex was first fitted into the cryo-EM density with a simple rigid body fitting and finally refined against the cryo-EM map. Unlike our observations in the OCS crystal structures, the cryo-EM map showed no density for any CTD, thus structural interpretation was limited to the analysis of the NTD arrangement (Supplementary Figure S3B). The root-mean-squares deviation (rmsd) between the refined cryo-EM and crystallographic model NTDs (based on C_α atoms of 2553 residues in total) was 1.26 Å, which indicates a high similarity between both models.

We further obtained cryo-EM structures of the tetrameric assembly and the OCS dimer (Figure 3B, left and central panel), which are however affected by anisotropic resolution due to preferred orientation of the respective particles. Therefore, we performed rigid body fitting of the available molecular model of the OCS dimers and did not attempt further model refinement. In summary, the distribution of these oligomeric states in solution indicates the tight OCS dimer as the basic building block. The tight dimers further oligomerize in a cyclic sequential manner via a single salt bridge towards the formation of the hexameric assembly (Figure 3C).

Interestingly, we observed tetramers and hexamers only in cryo-EM samples and exclusively dimers during negative stain EM, that is typically performed at much lower concentrations (Supplementary Figure S4A–B). Chemical crosslinking before negative stain EM stabilized the hexameric horseshoe-like conformation (Supplementary Figure S4C–D). These observations suggest that the protein might be prone to stepwise concentration-dependent self-association of OCS homodimers rather than concerted hexameric assembly.

To further characterize OCS dimer self-association, we analyzed OCS (*wt*) and the OCS (KD) variant at different concentrations by SAXS (Supplementary Table S3). OCS (*wt*) SAXS profiles show indeed a concentration-dependent change in the scattering intensities, as the sample was diluted from 7 to 0.5 mg/mL (Figure 4A, Supplementary Figure S5A). These changes correlate to a decrease in the apparent molecular weight (MW) and radius of gyration (R_g) of the particle population, consistent with mixtures of tetramers and hexamers, as observed in the cryo-EM samples (Figure 4B, Supplementary Figure S5C–D). These observations for OCS (*wt*) contrast with those for OCS (KD) mutant, where the SAXS profiles and the corresponding MW and R_g as well as other structural parameters such as the Porod volume and real-space scattering-pair distance distribution are consistent with OCS dimers throughout the concentration series (Figure 4C–D, Supplementary Figure S5B–D). Indeed, by taking the X-ray crystal structures and subsequently including the mass and spatial disposition of both the NTD and CTD of each protomer in the OCS assemblies, the OCS (KD) mutant SAXS data is well described by the conformation of crystallographic dimer showing a χ^2 fit = 1.0 (Figure 4C) whereas the fit to the OCS (*wt*) SAXS data requires the application of a volume-fraction weighted ratio of crystallographic hexamers and tetramers at each sample concentration resulting in χ^2 fit range of 1.5–3.9 (Figure 4A–B).

To confirm the concentration-dependent change in OCS oligomeric state, we also performed SEC-MALS experiments using three different OCS (*wt*) injection corresponding to concentrations of 7, 2.5 and 0.5 mg/mL sample. We observed a decrease in MW averages obtained for decreasing OCS (*wt*) sample injection concentrations, while even at the highest sample injection concentration tested for the OCS (KD) variant the MW average showed that the mutant MW corresponds to a dimer (Figure 4D).

OCS oligomerization and thermostability

To investigate whether self-assembly of OCS dimers has an effect on thermostability, we determined the OCS (*wt*) and OCS (KD) variant unfolding temperatures using nanoscale Differential Scanning Fluorimetry (NanoDSF). While OCS (*wt*) unfolded at 43 °C, the dimeric OCS (KD) variant unfolded at 37 °C, corresponding to a reduction of 8 °C in melting temperature (Figure 4E, Supplementary Figure S6). This implies that self-assembly of OCS dimers has a protective effect on OCS unfolding. A second OCS unfolding event is independent on the type of OCS variant used and hence independent of the OCS oligomerization state (Supplementary Figure S6).

We finally tested whether lack of OCS dimer self-assembly impairs OCS catalytic activity, by monitoring ATP hydrolysis and AMP formation using reverse phase chromatography. As a negative control, we used an OCS K523A active site variant (Niebling et al. 2021), which was expected to be catalytically inactive, in analogy to an equivalent mutant of *A. thaliana* OCS (Supplementary Figure S7) (Fan et al. 2016). As we did not detect any significant difference in the AMP levels generated (Figure 4F–G), we concluded that lack of OCS self-assembly has no impact on OCS catalytic activity.

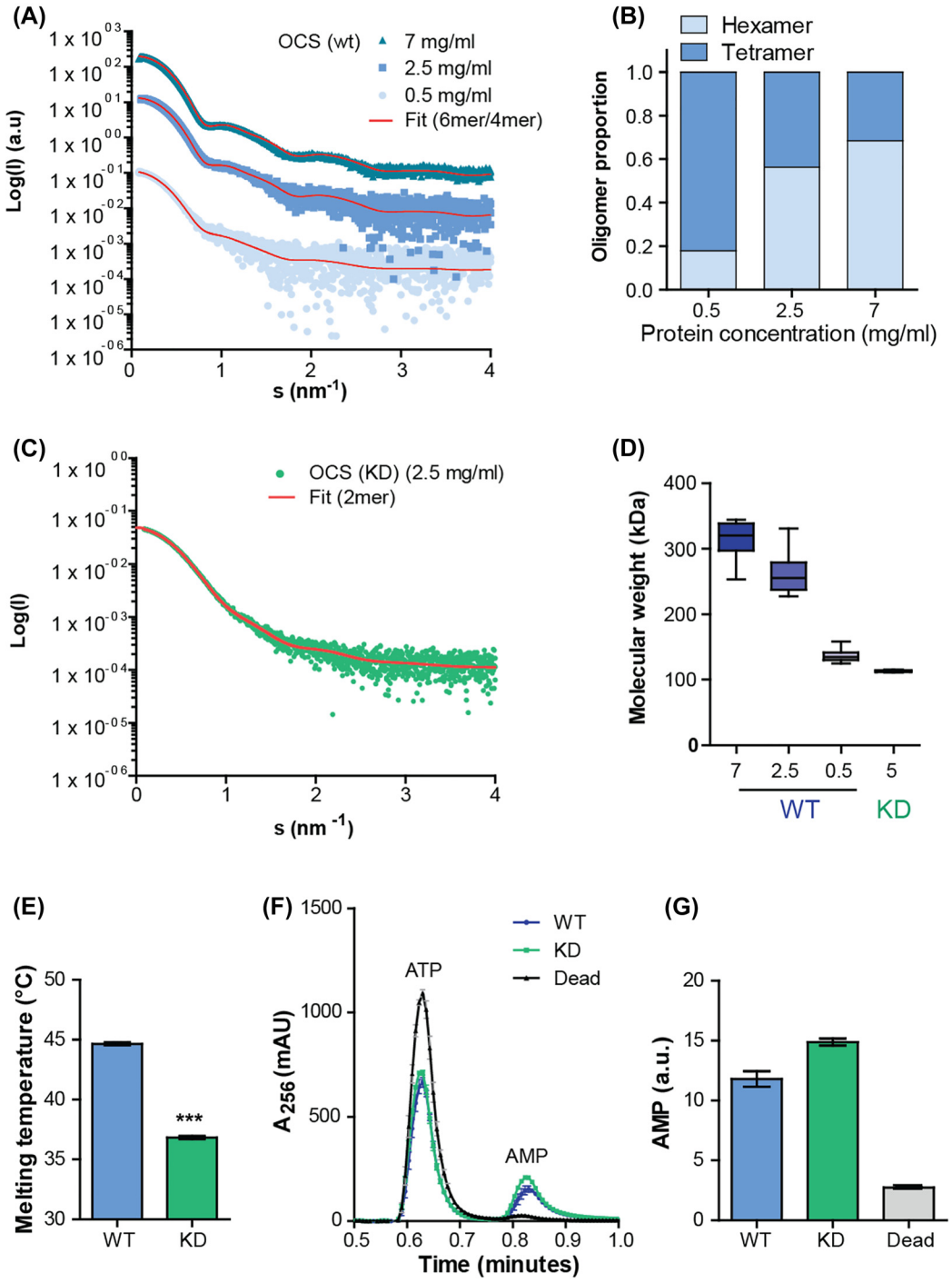

Figure 4: Biophysical and biochemical impact of concentration-dependent OCS assembly. (A) SAXS curves of OCS (*wt*) at different protein concentrations, with refined OCS tetramer/hexamer fit in red. Calculated χ^2 values are 3.9 for 7 mg/ml, 1.6 for 2.5 mg/ml and 1.2 for 0.5 mg/ml. The SAXS curves are vertically offset for clarity. (B) Estimation of OCS (*wt*) tetrameric/hexameric assembly ratio according to protein concentration. OCS (*wt*) shows a shift from hexamer to tetramer with decreasing sample concentration. (C) SAXS curve of the OCS (KD) variant at 2.5 mg/mL with a complete OCS dimer model fitted. The calculated χ^2 is 1.0. (D) Estimates of OCS (*wt*) and OCS (KD) MWs at different concentrations using SEC-MALLS. OCS (*wt*) shows a concentration-dependent change in MW, while OCS (KD) even at the highest concentration measured remains dimeric. (E) Melting temperatures of OCS (*wt*) and OCS (KD) measured by NanoDSF. OCS (KD) has a significantly lower melting temperature than OCS (*wt*). Measurements were carried out in triplicate. Student's *t*-test ***probability < 0.001. (F) Elution profile of 1 µM OCS (*wt*), OCS (KD) and OCS (K523A) catalytic reaction after 1 min with 100 µM oxalate. ATP and AMP elute at distinct times and OCS (K523A) mutant show no formation of AMP. (G) Quantification of AMP products. Measurements were carried out in triplicate.

Discussion

OCS is one of the most abundant proteins in yeast peroxisomes and comprises a PTS1 motif at its C-terminus (Blobel and Erdmann 1996). In contrast to the majority of other PTS1–containing peroxisomal targets, an OCS variant lacking the PTS1 is still capable of binding to the peroxisomal import receptor Pex5, indicating a second non-PTS1 receptor binding site (Hagen et al. 2015). To improve a mechanistic understanding of these findings, we compared the biophysical and structural properties of OCS from *S. cerevisiae* with the equivalent non-peroxisomal OCS from *A. thaliana*, presently the only other OCS with an experimental structure determined in a number of different ligand-bound and apo states (Fan et al. 2016).

The respective protomer structures can be superimposed with a root-mean-squares deviation (rmsd) of 1.8 Å for 418 matching residues of the NTD, which is equivalent to 96% of the complete NTD sequence (Supplementary Figure S8A). In the resulting structure-based sequence alignment 40% of all residues are identical (Supplementary Figure S7). Hence, it is not surprising that those parts of the structures of the two enzymes that are functionally important such as the active site are highly conserved (Supplementary Figure S9).

At level of enzyme protomers, we have noticed that the NTD/CTD arrangement in the *A. thaliana* enzyme and the most populated NTD/CTD arrangement of *S. cerevisiae* OCS are identical (Figure 3D, left panel; Supplementary Figure S8). In both structures, the arrangement is mediated by an invariant serine (Ser445 in the *S. cerevisiae* sequence), following the flexible NTD/CTD-connecting hinge sequence segment, which belongs to the most conserved sequence segments in the overall OCS alignment (Supplementary Figure S6). In the *A. thaliana* apo enzyme (PDB entry 5ie0), however, there is a tartrate ion bound into the enzyme's active site, which provides an additional specific interaction with K500 close to the C-terminus of the CTD (Supplementary Figure S8B). In contrast, in all yeast OCS structures presented in this contribution, no ligand was found in the active site and the C-terminal segment of the CTD, which includes the equivalent lysine (K523), remains unresolved. In summary, our data are suggestive that the NTD/CTD arrangement is dynamic, which is of functional importance irrespective of a specific organism and the absence or presence of a peroxisomal targeting signal. These findings are in-line with recent reviews on ANL indicating that CTD flexibility may be a general ANL property (Gulick 2009).

At the level of observed homo-dimeric assemblies, both enzymes form extensive assemblies by in part overlapping surfaces (Supplementary Figure S7). Surprisingly, at the level of residue-specific interactions, the two interfaces are not conserved, thus leading to dimeric arrangements with the second protomer in distinct orientations (Supplementary Figure S10). Finally, the most striking difference is in the ability of *S. cerevisiae* OCS to form concentration-dependent asymmetric hexameric assemblies. The key residues permitting this assembly (D36, K352) are conserved in some fungi species, such as filamentous fungi *Chaetomium thermophilum* and *Neurospora crassa* and candida species (*Candida glabrata*), but not in fission yeast (*Schizosaccharomyces pombe and japonicus*), *Yarrowia lipolytica* and in plants (*A. thaliana*) (Supplementary Figure S7). This may explain why such self-assembly property has not been observed for the *A. thaliana* enzyme. As the ability of forming higher order assemblies has been shown to be a property of the purified enzyme, it remains unknown whether such higher-order oligomerization is also formed under physiological conditions and possibly promotes translocation into yeast peroxisomes. In this model, the highly flexible and exposed PTS1 positions in oligomeric OCS would generate multiple PTS1-mediated Pex5 binding sites on the surface of hexameric OCS particles with overall dimensions of about 15 nm (Supplementary Figure S11). Future studies are required to unravel whether the presence of such arrangement with multiple Pex5 binding sites facilitates peroxisomal import. How PTS1-dependent and PTS1-independent binding to the peroxisomal Pex5 receptor share contributions to OCS peroxisomal translocation remains a fascinating research question as well.

Irrespective of its possible functional impact, our findings on asymmetric OCS assembly remain an unusual structural feature (Maksay and Marsh 2017; Marsh and Teichmann 2015). Although an increasing number of deviations to the original notion by Goodsell "*Asymmetric chitooligomers are virtually unknown*" (Goodsell and Olson 2000) have been found, the asymmetric self-association of OCS dimers remains a fascinating property of the *S. cerevisiae* enzyme. Taking our data together, whether and to what extent this collection of distinct properties provides any advantages to promote peroxisomal translocation remains subject of future research.

Materials and methods

Protein purification

Full-length *S. cerevisiae* OCS was cloned in a petM14 vector with an N-terminal hexa-histidine tag and a HRV3C protease cleavage site (www.embl.org/groups/protein-expression-purification). OCS was expressed

in autoinduction medium (Studier 2005), for 5 h at 37 °C and 26 h at 20 °C. Cells were harvested, resuspended in lysis buffer (50 mM Hepes (pH 7.5), 300 mM NaCl, 20 mM imidazole, protease inhibitor (Roche), DNAse (Sigma) and lysozyme (Sigma), homogenized for 1 h at 4 °C and lysed by sonication. Lysate was then cleared by centrifugation and the supernatant filtered at 0.45 µm and loaded onto Ni-NTA resin. Bound proteins were washed with 50 mM Hepes (pH 7.5), 500 mM NaCl, 20 mM imidazole. Protein was eluted with 50 mM Hepes (pH 7.5), 150 mM NaCl, 250 mM imidazole. The eluate was then dialyzed against Hepes (pH 7.5), 150 mM NaCl, 0.5 mM TCEP and simultaneously digested with 1 mg 3C-protease. Undigested protein and 3C-protease were removed by a second Ni-NTA step and flowthrough containing OCS was concentrated to 5 mL for subsequent gel filtration (Hiload 16/60 Superdex 200 pg, GE healthcare). Relevant fractions were pooled together, and the protein was concentrated, flash frozen in liquid nitrogen and stored at −80 °C. After 3C-protease cleavage, five additional residues (GPLGS) from the plasmid backbone remain at the OCS N-terminus.

Crystallization and X-ray structure determination

OCS (*wt*) was crystallized by vapor diffusion using conditions from the PEG I crystallization suite (Molecular Dimensions). OCS (*wt*) at a concentration of 6 mg/mL was crystallized in 0.2 M LiCl, 0.1 M Hepes (pH 8.0), 15% w/v PEG-3350. The OCS KD variant was crystallized in 0.15 M ammonium sulfate, 0.1 M MES (pH 6.0), 15% (w/v) PEG-4000. Crystals were soaked in cryo-solution, containing the crystallization mother liquor supplemented with 25% [v/v] ethylene glycol. Crystals were then mounted on cryo-loops (Hampton Research), and flash-cooled in liquid nitrogen. X-ray diffraction data of OCS (*wt*) and the OCS (KD) variant were collected on the synchrotron radiation beamlines MASSIF-1/ID30A-1 (ESRF, Grenoble) and EMBL P13 at PETRA III (EMBL/DESY, Hamburg), respectively. Data were processed using XDS (Kabsch 2010).

The OCS (*wt*) structure was solved by molecular replacement (MR) with PHASER (McCoy et al. 2007) using 4-Coumaroyl-CoA Ligase from *A. thaliana* (3TSY) as a search model. The initial MR solution was rebuilt interactively in COOT (Emsley et al. 2010). Each asymmetric unit contains 12 OCS protomers, grouped into two OCS hexamers, which are virtually identical in the OCS NTD arrangement. GESAMT (Krissinel 2012) superposes 2532 C-alpha atoms of the two hexamers NTD domains with rmsd of 0.525 Å. To simplify building CTD fragments that were relatively poorly resolved in the map, we used AlphaFold2 version 2.1.1 predicted structure (plddt > 90) (Supplementary Figure S12) (Jumper et al. 2021). The predicted CTD structure was rigid body fitted to the map and real space refined in COOT with self-restraints generated at 5 Å cut-off for all the chains. After subsequent refinement in REFMAC (Murshudov et al. 2011) version 5.8.0267 with NCS restrains and automatically defined TLS groups, CTDs with map cc's < 0.7 (CC_mask calculated using phenix.map_model_cc (Liebschner et al. 2019)) were completely removed from the model. From the remaining CTDs, residues without interpretable 2FoFc density at 1σ level were removed. The resulting model contained two OCS CTDs for the first hexamer and one CTD for the second hexamer (*cf.* Table 2). The final model was refined to R/Rfree of 0.23/0.25 at 2.87 Å resolution.

The OCS (KD) mutant structure was solved by MR with PHASER using the OCS (*wt*) NTD (residues 1–431) as a search model. The model was completed with AlphaFold2 predicted CTD structure and refined as described above. For the mutant structure we built a fragmented CTD for one out of two OCS chains in the asymmetric unit (*cf.* Table 2). The final model refined to R/Rfree of 0.21/0.25 at 2.45 Å resolution. Further details are summarized in Supplementary Table S1. The X-ray structures of OCS (*wt*) and OCS (KD) have been deposited in the Protein Data Bank with the following codes, respectively: 8AFF, 8AFG.

OCS interfaces were analyzed using the program PISA (Krissinel and Henrick 2007). Angles between OCS (*wt*) dimers were calculated using the PSICO (https://github.com/speleo3/pymol-psico) plugin in Pymol (PyMOL Molecular Graphics System, Version 2.0 Schrödinger, LLC). NTD/CTD arrangements were analyzed with the online version of DynDom (Hayward and Lee 2002; Veevers and Hayward 2019).

Negative stain EM

Four µL of OCS sample at a concentration of 0.003 mg/mL in TBS Buffer (50 mM Tris pH 8.0, 150 mM NaCl) was applied for 2 min on a freshly glow discharged carbon coated copper-grid (Agar scientific; G2400C) at room temperature. The sample was blotted with Whatman paper (No 5) and subsequently the grid was washed two times using 10 µL TBS buffer. A 10 µL drop of freshly prepared 0.75% uranyl formate solution was then applied on the grid for 30 s. Afterwards the excess of liquid was blotted away and the specimen was air-dried. Images were recorded with a JEM-1400 (JEOL) or a FEI Tecnai G2 Spirit (FEI) both equipped with LaB_6 cathode and a 4 K CMOS detector F416 (TVIPS). Single particles were selected using crYOLO (Wagner et al. 2019). Reference-free stable class-averages were computed using the ISAC approach of the SPHIRE software package (Moriya et al. 2017).

Crosslinking

Crosslinking with glutaraldehyde was performed in 50 mM Hepes (pH 8.0), 150 mM NaCl. Reaction mixtures with an amount of 0.003 mg/mL OCS were treated with 0.05% crosslinking reagent for 2 min and afterwards quenched by adding Tris (pH 8.0) to a final concentration of 100 mM. Prior to negative stain EM imaging, samples were purified via SEC using a Superose 6 Increase 5/150 GL.

Cryo-EM structure determination

For cryo-EM, 4 µL of sample at 0.3 mg/mL concentration was applied to freshly glow discharged holey carbon Quantifoil 2/1 grids (#EMS300-Cu). The sample was immediately blotted and plunged into liquid ethane cooled by liquid nitrogen using a Gatan Cryo-plunge 3 device at 95% humidity. The blotting time was 2.5 s at 25 °C (gentle blot). A cryo-EM dataset was collected with a C_s-corrected Titan Krios EM (ThermoFisher) equipped with a K2 direct electron detector (Gatan) and a quantum energy filter (Gatan). Movies were recorded in counting mode using the automated acquisition program EPU (ThermoFisher) at a magnification of 105,000x corresponding to a pixel size of 1.09 Å. 5594 movies were acquired in a defocus range of −0.7 to −2.2 µm. Each movie comprised 60 frames acquired over 12 s with a total dose of ~63 e/Å^2.

Monitoring of image collection as well as image pre-processing was performed using the TranSPHIRE software package (Stabrin et al. 2020). Motion correction was thereby performed on the fly using MotionCor2 (Zheng et al. 2017). The contrast transfer function was estimated using gCTF (Zhang 2016). Ten representative images were then manually picked using the crYOLO-box manager tool, to train crYOLO (Wagner et al. 2019) for further automated particle picking. A total of four million particles were finally selected and extracted using a box size of 182 pixels. SPHIRE

(1.0, 1.2, 1.3) (Wagner et al. 2019) was used for further single particle analysis steps. Multiple reference-free 2D classification rounds were then carried out, using the stable alignment and cluster approach (ISAC) (Yang et al. 2012) in SPHIRE (Supplementary Figure S7). After each round of 2D classification, we selected classes containing intact OCS populations, comprising OCS dimers, tetramers and hexamers. The resulting class averages were selected and subsequently used for VIPER (Penczek and Asturias 2014), to generate a low-resolution initial model. The respective class members for each oligomerization state were then subjected to 3D refinement in SPHIRE (Meridien) with C1 (dimeric and tetrameric particles) or C2 (hexameric particles) symmetry, imposed using the VIPER reconstruction as initial reference, respectively. The resulting projection parameters were used to re-center and re-extract the particles. The re-centered particles were again subjected to 3D refinements in SPHIRE (Meridien). Particle "polishing" was then performed using RELION (Zivanov et al. 2019). Final refinements were then performed in SPHIRE using the polished particles of each individual population, respectively. Fourier shell correlation analysis, 3D masking, sharpening and low-pass filtering were automatically performed using the PostRefiner tool of SPHIRE. Further details are given in Supplementary Table S2.

Cryo-EM maps and models were visualized using Chimera (Pettersen et al. 2004) and ChimeraX (Pettersen et al. 2021). Map segmentation was performed using the module Segment Map of the Chimera software package. Structure modeling of OCS was performed using COOT (Emsley et al. 2010). Real space refinement of the crystal structure in the EM density map was performed in PHENIX (Adams et al. 2011).

The resulting model coordinates are available in the Protein Data Bank with the PDB ID 8ATD. The cryo-EM maps have been deposited into the Electron Microscopy Data Bank with the ID EMD-15,646.

Small angle X-ray scattering analysis

Synchrotron SAXS data ($I(s)$ versus s, where $s = 4\pi\sin\theta/\lambda$, 2θ is the scattering angle and λ the X-ray wavelength, 0.124 nm) were measured from dialyzed solutions of OCS (*wt*) and OCS (KD) in 50 mM Hepes (pH 7.5), 150 mM NaCl, 0.5 mM TCEP at the EMBL P12 beam line at DESY (Blanchet et al. 2015) (Hamburg, Germany) using a Pilatus 6 M detector at a sample-detector distance of 3 m. OCS (*wt*) and OCS (KD) protein solutes at 7 or 5, 2.5 and 0.5 mg/mL concentrations were measured at 10 °C. A continuous flow 1 mm cell capillary was used to limit radiation damage. A total of 30 successive 0.1 s frames were collected for both the samples and the corresponding matched buffer. The process of 2D data reduction to generate 1D buffer-subtracted profiles was performed using the SASFLOW pipeline (Franke et al. 2012).

Data were analyzed using modules of the ATSAS 3.0.1 package (Franke et al. 2017). CRYSOL (Franke et al. 2017) was used to calculate the scattering profiles from the atomic coordinates of the OCS (*wt*) and OCS (KD) X-ray structures. CTDs were added to OCS protomers without CTDs modeled in the respective X-ray structures to create complete OCS model and fit them with the respective experimental SAXS data.

To characterize mixtures of the different oligomeric OCS species, the program OLIGOMER (Konarev et al. 2003) was used. It fits the observed experimental data by a weighted combination of the calculated model scattering curves (form factors) from different quaternary structures. The experimental SAXS data and models are deposited in SASBDB (Kikhney et al. 2020) (https://www.sasbdb.org/) with the accession codes SASDPV3, SASDPW3, SASDPX3, SASDPY3. Further details are presented in Supplementary Table S3.

Size-exclusion chromatography

Purified OCS (*wt*) and (KD) were analyzed by size-exclusion chromatography using a Superdex 200 Increase 10/300 GL (Cytiva) connected to a Aekta pure chromatography system. 200 µL of protein at 10 mg/mL were injected and analyzed at a flow of 0.5 mL/min. Injection of a standard (Bio-Rad) mixture of protein of known concentration and molecular weight (thyroglobin 670 kDa, γ-globin 158 kDa, ovalbumin 44 kDa, myoglobin 17 kDa and vitamin B_{12} 1.35 kDa) was used to estimate OCS (*wt*) and (KD) molecular weight.

Size-exclusion multi angle light scattering

Protein mass measurements were performed on an Agilent HPLC system connected to a MiniDAWN® TREOS® multi-angle laser light scattering detector (MALS), with an Optilab T-rEX (RI) refractometer (Wyatt, Germany). 50 µL of sample at 10, 5, 1 mg/mL for OCS (*wt*) or 5 mg/mL for OCS (KD) were loaded onto a Superdex 200 Increase 5/150 GL (Cytiva) and the MALLS and RI measurements were performed at 25 °C, where the refractive index increment (dn/dc) of the protein samples was set to 0.185 mL/g. The data were processed using Wyatt ASTRA 7.0.1 software (Wyatt).

Nano differential scanning fluorimetry

Melting temperature were measured by NanoDSF using a Nanotemper Prometheus NT.48. Tryptophan intrinsic fluorescence emission was recorded at 330 and 350 nm with 30% excitation power during thermal ramping from 20 °C to 90 °C at a ramping velocity of 1 °C per minute. A volume of 10 µL OCS in 50 mM Hepes (pH 7.5), 150 mM NaCl, 0.5 mM TCEP and at a concentration of 1 mg/mL were loaded in NanoDSF grade standard capillaries. Samples were measured in triplicates and the calculated melting temperatures averaged. Melting temperature were calculated by the software PR. ThermControl (Nanotemper).

Enzymatic activity assay

Enzymatic activity was measured by AMP production at 254 nm after 60 s reaction at 25 °C. The sample volume was 40 µL, containing 50 mM Hepes (pH 7.5), 150 mM NaCl, 2 mM $MgCl_2$, 0.3 mM CoA, 0.4 mM ATP and 1 µM OCS (*wt*), OCS (KD) or OCS (K523A, negative control), supplemented with 100 µM oxalate. Reactions were stopped by adding 10 µL of 1 mM HCl and kept on ice. Reaction tubes were centrifuged for 10 min at 4 °C, 14,000 rpm on a tabletop centrifuge to remove aggregated proteins and then sequentially injected into an HPLC (Agilent) equipped with a C18 analytical column (Agilent Poroshell 120).

For high-performance liquid chromatography analysis, solvent A was 50 mM ammonium acetate (pH 5.0) and solvent B was 100% methanol. The flow rate was kept at 1 mL/min and at room temperature. Samples were kept at 10 °C in a 96 well V-bottom plate and sealed to avoid evaporation. The elution method consisted of 0% solvent B for 5 min and then a continuous gradient from 0% to 70% of solvent B for 15 min, and then 100% solvent B for 5 min and re-equilibration of the column in solvent A. Samples with only ATP, AMP and CoA were analyzed to define the elution time of each component. AMP production was assessed by measuring the area under the curve between 0.75 and 1.00 min of elution. Curves were integrated using GraphPad Prism. All reactions were run in triplicate.

Author contributions: JB, EAG, PL, CG and MW designed the project. JB, EAG, PL performed the experiments. JB, PL, CMJ, GC, CG and MW analyzed the data. JB, PL, CG, CMJ, and MW wrote the manuscript. SR, CG and MW supported the project.
Research funding: This project has been supported by FOR 1905 (PerTrans consortium) GA 2519/1–2 to C.G, RA 1781/4-2 to S.R, and 1058/9-1 and 1058/9-2 to M.W from the German Research Foundation (DFG). J. B. has been supported by the Marie Skłodowska-Curie Actions program (grant # 664726) from the European Commission. E.-A. has been supported by the Marie Curie Initial Training Network 'PERFUME-ITN' (grant # 316723) from the European Commission. Synchrotron, SAXS and X-ray diffraction data were collected at beamlines P12 and P13 operated by the EMBL Hamburg Unit at the PETRA III storage ring (DESY, Hamburg, Germany) as well as on beamline ID30A-1 at the European Synchrotron Radiation Facility (ESRF), Grenoble, France, respectively. We thank for technical support by Stephan Niebling from the SPC facility at EMBL Hamburg Unit. We thank D. Prumbaum and O. Hofnagel (Max Planck Institute of Molecular Physiology, Dortmund) for assistance in cryo-EM data collection. We thank Claudia Litz for her experimental assistance.
Conflict of interest statement: The authors declare no conflicts of interest regarding this article.

References

Adams, P.D., Afonine, P.V., Bunkóczi, G., Chen, V.B., Echols, N., Headd, J.J., Hung, L.W., Jain, S., Kapral, G.J., Grosse, K, et al. (2011). The Phenix software for automated determination of macromolecular structures. Methods 55: 94–106.

Blanchet, C.E., Spilotros, A., Schwemmer, F., Graewert, M.A., Kikhney, A., Jeffries, C.M., Franke, D., Mark, D., Zengerle, R., Cipriani, F., et al. (2015). Versatile sample environments and automation for biological solution X-ray scattering experiments at the P12 beamline (PETRA III, DESY). J. Appl. Crystallogr. 48: 431–443.

Blobel, F. and Erdmann, R. (1996). Identification of a yeast peroxisomal member of the family of AMP-binding proteins. Eur. J. Biochem. 240: 468–476.

Emsley, P., Lohkamp, B., Scott, W.G., and Cowtan, K. (2010). Features and development of coot. Acta Crystallogr. D Biol. Crystallogr. 66: 486–501.

Fan, M., Xiao, Y., Li, M., and Chang, W. (2016). Crystal structures of *Arabidopsis thaliana* oxalyl-CoA synthetase essential for oxalate degradation. Mol. Plant 9: 1349–1352.

Foster, J. and Nakata, P.A. (2014). An oxalyl-CoA synthetase is important for oxalate metabolism in Saccharomyces cerevisiae. FEBS Lett. 588: 160–166.

Franke, D., Petoukhov, M.V., Konarev, P.V., Panjkovich, A., Tuukkanen, A., Mertens, H.D.T., Kikhney, A.G., Hajizadeh, N.R., Franklin, J.M., Jeffries, C.M., et al. (2017). Atsas 2.8: a comprehensive data analysis suite for small-angle scattering from macromolecular solutions. J. Appl. Crystallogr. 50: 1212–1225.

Franke, D., Kikhney, A.G., and Svergun, D.I. (2012). Automated acquisition and analysis of small angle X-ray scattering data. Nucl. Instrum. Methods Phys. Res. Sect. A Accel. Spectrom. Detect. Assoc. Equip. 689: 1–114.

Goldsmith, M., Barad, S., Knafo, M., Savidor, A., Ben-Dor, S., Brandis, A., Mehlman, T., Peleg, Y., Albeck, S., Dym, O., et al. (2022). Identification and characterization of the key enzyme in the biosynthesis of the neurotoxin β-ODAP in grass pea. J. Biol. Chem. 298: 101806.

Goodsell, D.S. and Olson, A.J. (2000). Structural symmetry and protein function. Annu. Rev. Biophys. Biomol. Struct. 29: 105–153.

Gulick, A.M. (2009). Conformational dynamics in the acyl-CoA synthetases, adenylation domains of non-ribosomal peptide synthetases, and firefly luciferase. ACS Chem. Biol. 4: 811–827.

Gulick, A.M., Starai, V.J., Horswill, A.R., Homick, K.M., and Escalante-Semerena, J.C. (2003). The 1.75 Å crystal structure of acetyl-CoA synthetase bound to adenosine-5'-propylphosphate and coenzyme A. Biochemistry 42: 2866–2873.

Hagen, S., Drepper, F., Fischer, S., Fodor, K., Passon, D., Platta, H.W., Zenn, M., Schliebs, W., Girzalsky, W., Wilmanns, M., et al. (2015). Structural insights into cargo recognition by the yeast PTS1 receptor. J. Biol. Chem. 290: 26610–26626.

Hayward, S. and Lee, R.A. (2002). Improvements in the analysis of domain motions in proteins from conformational change: DynDom version 1.50. J. Mol. Graph. Model. 21: 181–183.

Jumper, J., Evans, R., Pritzel, A., Green, T., Figurnov, M., Ronneberger, O., Tunyasuvunakool, K., Bates, R., Žídek, A., Potapenko, A., et al. (2021). Highly accurate protein structure prediction with AlphaFold. Nature 596: 583–589.

Kabsch, W. (2010). Integration, scaling, space-group assignment and post-refinement. Acta Crystallogr. D Biol. Crystallogr. 66: 133–144.

Kikhney, A.G., Borges, C.R., Molodenskiy, D.S., Jeffries, C.M., and Svergun, D.I. (2020). SASBDB: towards an automatically curated and validated repository for biological scattering data. Protein Sci. 29: 66–75.

Konarev, P.V., Volkov, V.V., Sokolova, A.V., Koch, M.H.J., and Svergun, D.I. (2003). PRIMUS: a Windows PC-based system for small-angle scattering data analysis. J. Appl. Crystallogr. 36: 1277–1282.

Krissinel, E. (2012). Enhanced fold recognition using efficient short fragment clustering. J. Mol. Biochem. 1: 76–85.

Krissinel, E. and Henrick, K. (2007). Inference of macromolecular assemblies from crystalline state. J. Mol. Biol. 372: 774–797.

Lee, R.A., Razaz, M., and Hayward, S. (2003). The DynDom database of protein domain motions. Bioinformatics 19: 1290–1291.

Liebschner, D., Afonine, P.V., Baker, M.L., Bunkóczi, G., Chen, V.B., Croll, T.I., Hintze, B., Hung, L.W., Jain, S., Mccoy, A.J., et al. (2019). Macromolecular structure determination using X-rays, neutrons and electrons: recent developments in Phenix. Acta Crystallogr. D Struct. Biol. 75: 861–877.

Maksay, G. and Marsh, J.A. (2017). Signalling assemblies: the odds of symmetry. Biochem. Soc. Trans. 45: 599–611.

Marsh, J.A. and Teichmann, S.A. (2015). Structure, dynamics, assembly, and evolution of protein complexes. Annu. Rev. Biochem. 84: 551–575.

Mccoy, A.J., Grosse-Kunstleve, R.W., Adams, P.D., Winn, M.D., Storoni, L.C., and Read, R.J. (2007). Phaser crystallographic software. J. Appl. Crystallogr. 40: 658–674.

Moriya, T., Saur, M., Stabrin, M., Merino, F., Voicu, H., Huang, Z., Penczek, P.A., Raunser, S., and Gatsogiannis, C. (2017). High-resolution single particle analysis from electron cryo-microscopy images using SPHIRE. J. Vis. Exp. 6: 55448.

Murshudov, G.N., Skubák, P., Lebedev, A.A., Pannu, N.S., Steiner, R.A., Nicholls, R.A., Winn, M.D., Long, F., and Vagin, A.A. (2011). REFMAC5 for the refinement of macromolecular crystal structures. Acta Crystallogr. D Biol. Crystallogr. 67: 355–367.

Niebling, S., Burastero, O., Bürgi, J., Günther, C., Defelipe, L.A., Sander, S., Gattkowski, E., Anjanappa, R., Wilmanns, M., Springer, S., et al. (2021). FoldAffinity: binding affinities from nDSF experiments. Sci. Rep. 11: 9572.

Penczek, P.A. and Asturias, F.J. (2014). Ab initio cryo-EM structure determination as a validation problem. In: *IEEE international conference on image processing*. ICIP.

Pettersen, E.F., Goddard, T.D., Huang, C.C., Couch, G.S., Greenblatt, D.M., Meng, E.C., and Ferrin, T.E. (2004). UCSF Chimera–a visualization system for exploratory research and analysis. J. Comput. Chem. 25: 1605–1612.

Pettersen, E.F., Goddard, T.D., Huang, C.C., Meng, E.C., Couch, G.S., Croll, T.I., Morris, J.H., and Ferrin, T.E. (2021). UCSF ChimeraX: structure visualization for researchers, educators, and developers. Protein Sci. 30: 70–82.

Stabrin, M., Schoenfeld, F., Wagner, T., Pospich, S., Gatsogiannis, C., and Raunser, S. (2020). TranSPHIRE: automated and feedback-optimized on-the-fly processing for cryo-EM. Nat. Commun. 11: 5716.

Studier, F.W. (2005). Protein production by auto-induction in high density shaking cultures. Protein Expr. Purif. 41: 207–234.

Veevers, R. and Hayward, S. (2019). Methodological improvements for the analysis of domain movements in large biomolecular complexes. Biophys. Physicobiol. 16: 328–336.

Wagner, T., Merino, F., Stabrin, M., Moriya, T., Antoni, C., Apelbaum, A., Hagel, P., Sitsel, O., Raisch, T., and Prumbaum, D. (2019). SPHIRE-crYOLO is a fast and accurate fully automated particle picker for cryo-EM. Commun. Biol. 2: 218.

Williams, H.E. and Smith, L.H., Jr. (1968). Disorders of oxalate metabolism. Am. J. Med. 45: 715–735.

Yang, Z., Fang, J., Chittuluru, J., Asturias, F.J., and Penczek, P.A. (2012). Iterative stable alignment and clustering of 2D transmission electron microscope images. Structure 20: 237–247.

Zhang, K. (2016). Gctf: real-time CTF determination and correction. J. Struct. Biol. 193: 1–12.

Zheng, S.Q., Palovcak, E., Armache, J.P., Verba, K.A., Cheng, Y., and Agard, D.A. (2017). MotionCor2: anisotropic correction of beam-induced motion for improved cryo-electron microscopy. Nat. Methods 14: 331–332.

Zivanov, J., Nakane, T., and Scheres, S.H.W. (2019). A Bayesian approach to beam-induced motion correction in cryo-EM single-particle analysis. IUCr J 6: 5–17.

Supplementary Material: This article contains supplementary material (https://doi.org/10.1515/hsz-2022-0273).